MODELING OBSERVED DECAY-LESS OSCILLATIONS AS RESONANTLY ENHANCED KELVIN–HELMHOLTZ VORTICES FROM TRANSVERSE MHD WAVES AND THEIR SEISMOLOGICAL APPLICATION

P. Antolin[1,2], I. De Moortel[1], T. Van Doorsselaere[3], and T. Yokoyama[4]

[1] School of Mathematics and Statistics, University of St. Andrews, St. Andrews, Fife KY16 9SS, UK; patrick.antolin@st-andrews.ac.uk
[2] National Astronomical Observatory of Japan, Osawa, Mitaka, Tokyo 181-8588, Japan
[3] Centre for mathematical Plasma Astrophysics, Mathematics Department, KU Leuven, Celestijnenlaan 200B bus 2400, B-3001 Leuven, Belgium
[4] Department of Earth and Planetary Science, The University of Tokyo, Hongo, Bunkyo-ku, Tokyo 113-0033, Japan

ABSTRACT

In the highly structured solar corona, resonant absorption is an unavoidable mechanism of energy transfer from global transverse MHD waves to local azimuthal Alfvén waves. Due to its localized nature, direct detection of this mechanism is extremely difficult. Yet, it is the leading theory explaining the observed fast damping of the global transverse waves. However, at odds with this theoretical prediction are recent observations that indicate that in the low-amplitude regime such transverse MHD waves can also appear decay-less, a still unsolved phenomenon. Recent numerical work has shown that Kelvin–Helmholtz instabilities (KHI) often accompany transverse MHD waves. In this work, we combine 3D MHD simulations and forward modeling to show that for currently achieved spatial resolution and observed small amplitudes, an apparent decay-less oscillation is obtained. This effect results from the combination of periodic brightenings produced by the KHI and the coherent motion of the KHI vortices amplified by resonant absorption. Such an effect is especially clear in emission lines forming at temperatures that capture the boundary dynamics rather than the core, and reflects the low damping character of the local azimuthal Alfvén waves resonantly coupled to the kink mode. Due to phase mixing, the detected period can vary depending on the emission line, with those sensitive to the boundary having shorter periods than those sensitive to the loop core. This allows us to estimate the density contrast at the boundary.

Key words: magnetohydrodynamics (MHD) – Sun: activity – Sun: corona – Sun: oscillations

1. INTRODUCTION

In the last decade research has shown that waves and oscillations permeate the solar atmosphere and constitute coronal heating candidates. Of particular interest among these waves are transverse MHD waves. Their characteristic fast damping, particularly for strong amplitudes (Aschwanden et al. 1999; Nakariakov et al. 1999; Arregui et al. 2012; De Moortel & Nakariakov 2012; Verwichte et al. 2013; Goddard & Nakariakov 2016), is successfully explained by resonant absorption and mode coupling.

Resonant absorption (or mode coupling for propagating waves) is an ideal process of energy transfer between different wave modes (Ionson 1978; Goossens et al. 2002, 2011; Pascoe et al. 2010; De Moortel et al. 2016) that has been shown to be very efficient and robust (Terradas et al. 2008b; Pascoe et al. 2011; De Moortel & Nakariakov 2012). This mechanism predicts that in the classical picture of coronal loops with a smooth density gradient between the inside and the outside of the flux tube, the global transverse mode can resonantly couple to local Alfvén waves of azimuthal character. The global transverse mode, which consists of a purely transverse displacement of the loop core, then behaves as azimuthal Alfvén waves at the boundary for most of the oscillation time. This means that most of the displacement (and thus the energy) in such waves is azimuthal and local rather than transverse and global, making resonant absorption extremely difficult to observe directly.

Recently, decay-less transverse oscillations have been reported (Anfinogentov et al. 2013, 2015; Nisticò et al. 2013; Goddard et al. 2016), apparently at odds with resonant absorption theory. These events have a rather ubiquitous character in active regions and correspond well to fundamental (standing) kink modes. The clearly decay-less cases seem to occur on long loops with small perturbation amplitudes that on average are less than 1% of the kink speed.

Numerical simulations in 3D MHD have shown that transverse MHD waves can become unstable to Kelvin–Helmholtz instabilities (KHI), due to shear motions at the boundary of flux tubes (Karpen et al. 1993; Ofman et al. 1994; Poedts et al. 1997; Terradas et al. 2008a; Antolin et al. 2014; Zaqarashvili et al. 2015). The KHI associated with transverse MHD waves leads to the generation of a myriad of vortices and current sheets along the flux tube, so-called TWIKH (Transverse Wave Induced Kelvin–Helmholtz) rolls. The mixing and the heating produced by the KHI, combined with the compressive nature of the vortices, leads to strand-like structure in intensity images in coronal loops (Antolin et al. 2014), and thread-like structure in prominences (Antolin et al. 2015). Furthermore, the combination of resonant absorption (and phase mixing) and the KHI leads to anti-phase behavior between the line of sight (LOS) velocity and the (transverse) plane-of-the-sky (POS) motion, a characteristic observed recently in a prominence by *Hinode*/SOT and *IRIS* (Okamoto et al. 2015).

Here we show that the combination of resonant absorption and the KHI can be readily seen in current coronal imaging instruments as small amplitude decay-less transverse oscillations, thus providing an explanation for the recent observations. We further demonstrate a potential MHD seismology application.

2. NUMERICAL MODEL

Our 3D MHD numerical model is the same as in Antolin et al. (2014), where we take a loop with a density and

temperature contrast with respect to the ambient low-β coronal atmosphere. The loop is initially in hydrostatic equilibrium and has density and temperature ratios $\rho_i/\rho_e = 3$ and $T_i/T_e = 1/3$, respectively, where the index i (e) denotes internal (external) values. The magnetic field is uniformly set to $B = 22.8$ G. We initially take $T_i = 10^6$ K, and $\rho_i = 3 \times 10^9$ μm_p g cm^{-3} ($\mu = 0.5$, and m_p is the proton mass). The loop boundary has a width of $\ell/R \approx 0.4$, where R is the radius of the loop. The length L of the loop is $200\,R$, and we set $R = 1$ Mm.

The loop is subject to a perturbation mimicking a fundamental kink mode (longitudinal wavenumber $kR = \pi R/L \approx 0.015$) with an initial amplitude of $v_0 = 0.05\,c_s$, with c_s as the external sound speed. This corresponds to $v_0 = 15$ km s^{-1} in our model. The corresponding kink phase speed is $c_k \approx 1574$ km s^{-1}. For further details please refer to Antolin et al. (2014).

We perform the 3D MHD simulation described above with the CIP-MOCCT scheme (Kudoh et al. 1999), including constant resistivity and viscosity. The MHD equations are solved, excluding gravity and loop curvature, which are second-order factors for the present work. Furthermore, the effects of radiative cooling and thermal conduction are also neglected, as they are expected to be unimportant due to their longer timescales compared to that of the kink wave period.

The numerical box is $512 \times 256 \times 50$ points in the x, y, and z directions, respectively, where (x, y) denote the transverse plane to the loop axis (along z) and x is the direction of oscillation. Thanks to the symmetric properties of the kink mode, only half the plane in y and half the length of the loop are modeled (from $z = 0$ to $z = 100\,R$), and we set symmetric boundary conditions in all boundary planes except for the x boundary planes, where periodic boundary conditions are imposed. In order to minimize the influence from side boundary conditions (along x and y), the spatial grids in x and y are non-uniform, with exponentially increasing values for distances well beyond the maximum displacement. The maximum distance in x and y from the center is $\approx 16\,R$. The spatial resolution at the loop's location is $0.0156\,R = 15.6$ km. From a parameter study, we estimate that the effective (combined explicit and numerical) Reynolds and Lundquist numbers in the code are of the order of $10^4 - 10^5$.

3. NUMERICAL RESULTS AND FORWARD MODELING

3.1. A Dual Mechanism Leading to Strand-like Structure in EUV Emission Lines

Following the initial perturbation, the loop starts oscillating with a period $P = 256$ s, closely corresponding to the period of the fundamental mode $2L/c_k$. The maximum displacement of the loop is 440 km ($0.44\,R$), leading to a transverse velocity of 6.9 km s^{-1}.

The kink mode produces a velocity shear at the boundary of the flux tube, particularly between the amplified (azimuthal) resonant flow and the purely transverse motion of the kink mode, which generates the KHI. The KHI enhances the mixing with the external plasma and the viscous and magnetic dissipation of the kinetic and magnetic energy from the narrow resonant region. TWIKH rolls occur all along the flux tube in a roughly synchronized manner and are able to compress the plasma. They therefore significantly deform the density and temperature structure in the transverse plane of the flux tube. Such vortices are therefore regions of enhanced emissivity,

resulting in clear strand-like structure in EUV intensity images of the loop, as first shown in Antolin et al. (2014; and thread-like structure in chromospheric conditions, Antolin et al. 2015).

3.2. Emission Lines, LOS, and Resolution

For comparison with observations we forward model the results from the numerical simulation into observable quantities using the FoMo code (Van Doorsselaere et al. 2016). We take the LOS plane perpendicular to the loop axis and define the LOS angle such that $0°$ is perpendicular to the axis of oscillation. We choose the Fe IX 171 Å and Fe XII 193 Å emission lines, which have maximum formation temperatures of $\log T = 5.9$ and $\log T = 6.2$, respectively. Accordingly, in this particular model, the Fe IX 171 Å line is more tuned to detect the plasma response at the core of the loop, while the Fe XII 193 Å line is more sensitive to the hotter plasma near the boundaries (right panels of Figure 1). From here on, we refer to the Fe IX 171 Å line as the core line, and the Fe XII 193 Å line as the boundary line.

For correct comparison with observations with a given instrument with a resolving power of X (defined as the FWHM of the PSF and we take the plate-scale equal to half the spatial resolution) we degrade the original spatial resolution of the numerical model by first convolving the image of interest with a Gaussian with an FWHM of X. We then resample the data according to the specific pixel size of the target instrument and add photon noise (Poisson-distributed).

3.3. EUV Variability

Bright oscillatory strand-like structures are noticeable in Figure 1 in both emission lines after about 2 periods, corresponding to the formation of TWIKH rolls. The amount of strand-like structure is largest in the boundary line. The overall damping of the kink mode is clear in Fe IX 171 Å. However, in Fe XII 193 Å, it becomes hard to discern, partly because of the large amount of fine-scale structure produced by the TWIKH rolls. A careful look into this substructure reveals inner oscillations damping to a much weaker extent.

While the loop is observed becoming thinner ($\approx 15\%$) and dimmer ($\approx 20\%$) in time in Fe IX 171 Å, in Fe XII 193 Å the loop becomes broader ($\approx 25\%$) and significantly brighter ($\approx 100\%$). The brightness increase and broadening occurs rapidly, in about one period after the onset of the KHI. Periodic brightening is also observed, mostly in the boundary line close to the edges of the loop. These localized enhancements, caused by LOS superposition of the TWIKH rolls, perturb the overall intensity trend by about 1.5% and 0.2% for Fe XII and Fe IX, respectively.

3.4. Imaging Characteristics at Low Spatial Resolution and Different LOS

As the spatial resolution is degraded, Figure 2 shows that the fine-scale strand-like structure completely vanishes for a resolved spatial scale of $0.5\,R$, although some features can still be noticed in the boundary line. For lower spatial resolutions, only the intensity variation and overall damping behavior of the kink mode are observed. Contrary to the core line, in the boundary line, besides the brightening the damping appears negligible. The apparent decay-less oscillation can appear non-sinusoidal, which is particularly clear in the third right panel
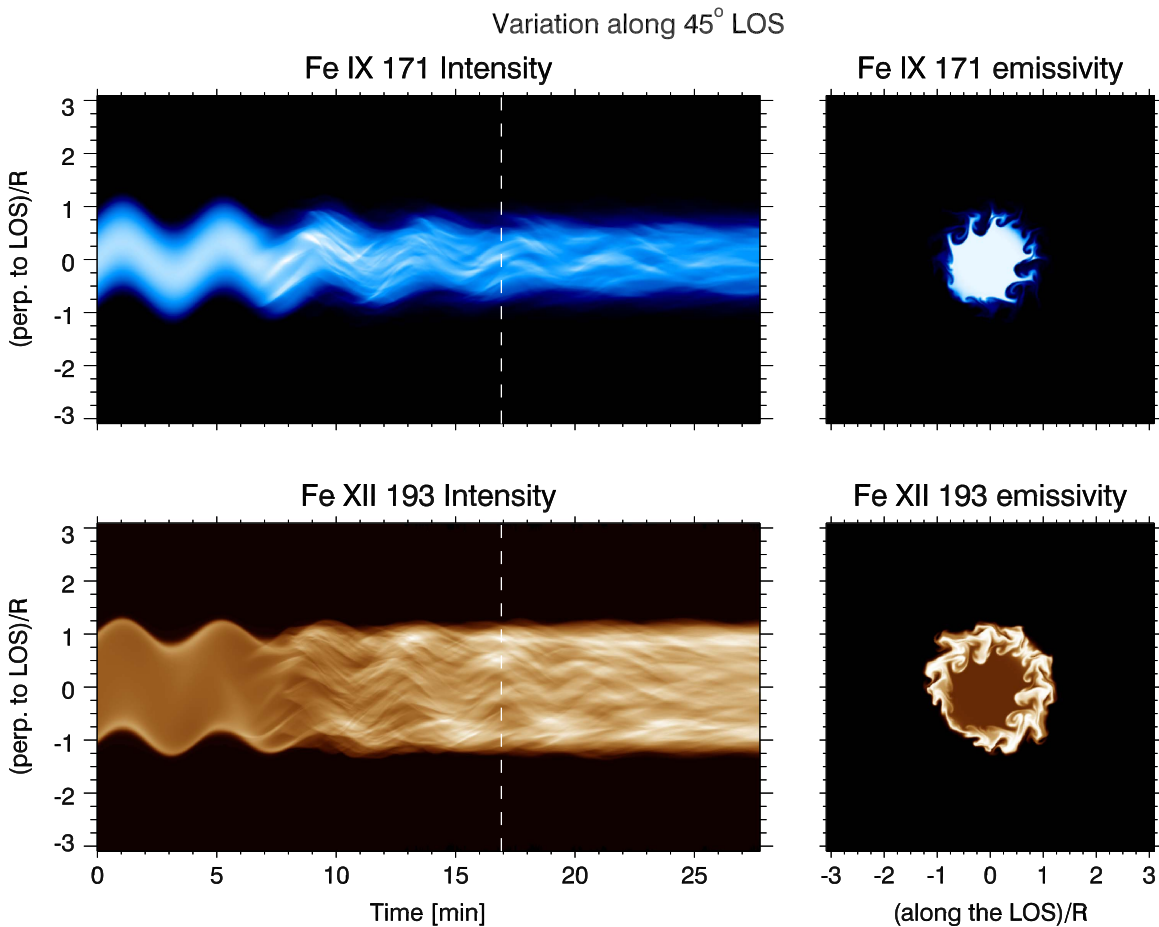
Figure 1. Left panels: time–distance diagrams of the forward modeling of the numerical model in the Fe IX 171 Å (in blue, top panel) and Fe XII 193 Å (in brown, bottom panel) intensity for a slit placed perpendicular at the apex of the loop, at a 45° LOS angle and at numerical (highest) spatial resolution. Right panels: snapshot of the cross-section of the emissivity for each line ($G_\lambda(T, n_e)n_e^2$, with G as the contribution function and n_e as the electron density) for the time indicated by the dashed line in the time–distance diagrams. The cross-section is rotated by the same LOS angle.

from the top in Figure 2 in the first four oscillations. Figure 3 shows that these effects are independent of the LOS angle.

To further improve comparison with *SDO*/AIA observations, we convolve and rebin the results to achieve a spatial resolution of 1″2 (as explained in Section 3.2). As can be seen in Figure 4, the overall intensity variation, the damping in the core line, and decay-less oscillation in the boundary line can still be clearly observed. The observed displacements of the loop in the core and boundary lines are 370 and 230 km, respectively.

In the bottom panel of Figure 4 we note that the boundary line profile starts oscillating in-phase with the core line and the density but goes quickly out-of-phase, an effect clearly noticeable after two periods. In particular, the oscillatory profile of the core line goes above 90° out-of-phase with the boundary line after about four periods. The fits to the core and boundary lines give periods of 258 and 240 s, respectively. The fit to the density gives a period of 253 s.

4. DISCUSSION AND CONCLUSIONS

In this paper, we have investigated imaging signatures of the transverse MHD wave derived from 3D MHD numerical simulations and forward modeling. The main factors affecting the intensity modulation in the host loops are the KHI and resonant absorption. Importantly, the KHI vortices (TWIKH

rolls) carry over characteristics of the resonant absorption and phase mixing mechanisms, allowing these to be detected with current instrumentation. We have found that the KHI produces significant intensity changes and that emission lines with different temperature sensitivity to either the loop core or the external medium provide insights into different wave modes.

At a high spatial resolution and especially in the hot line, the fine strand-like structure generated by the TWIKH rolls can be observed, as described in Antolin et al. (2014). At a lower spatial resolution corresponding to AIA, we have shown that the detected damping and period can vary depending on the emission line, which can lead to an out-of-phase behavior between the core and boundary lines. These results can be understood from the fact that the boundary line is more sensitive to the KHI dynamics, to resonant absorption and phase mixing. A decay-less oscillation is obtained in the boundary line for any LOS angle and this is the result of periodic brightenings and the coherent motion of the vortices. The vortices, in turn, result from unstable azimuthal Alfvén waves. Therefore, this decay-less oscillation is more reflective of the Alfvén waves coupled resonantly to the kink mode than the global kink mode itself. Resonant absorption transfers the energy of the kink mode to the Alfvén waves, whose dampings are expected to be much lower than that of the kink mode, since they rely on phase mixing and the turbulence resulting from the
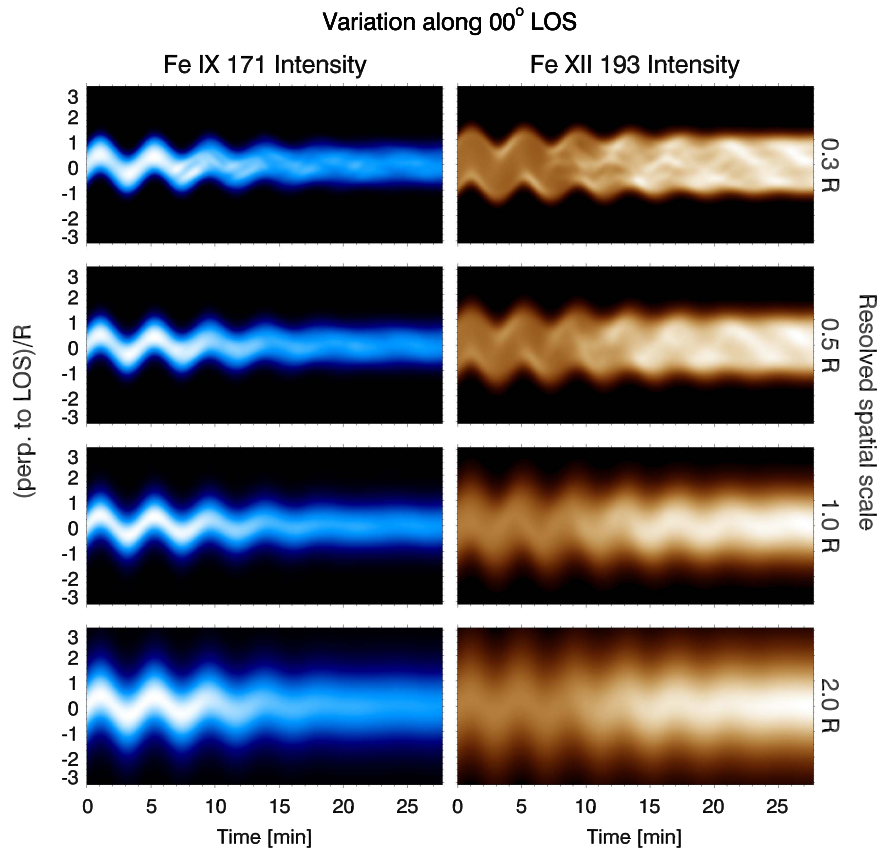
Figure 2. Time–distance diagram of the Fe IX (left column) and Fe XII (right column) intensities for the same configuration as in Figure 1, but for a 0° LOS and different spatial resolution (indicated on the right side axis of the right column), obtained through Gaussian convolution only (see Section 3.2 for details).
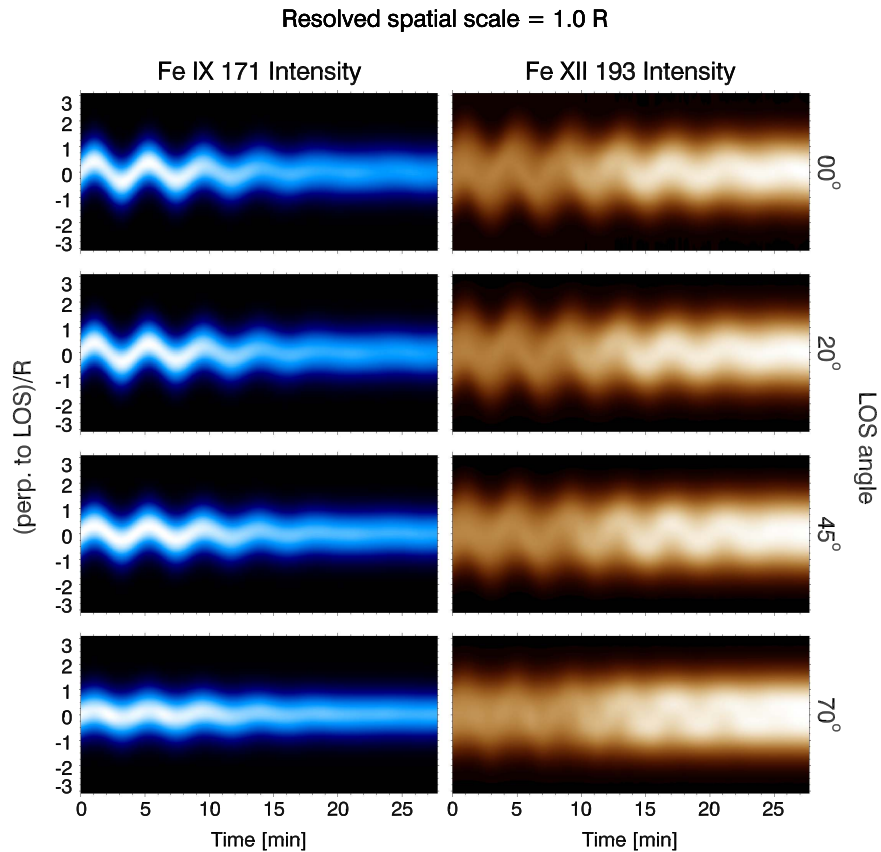

Figure 3. Similar to Figure 2, but for a fixed spatial resolution of 1 *R* and various LOS angles (indicated on the right side axis of the right column).
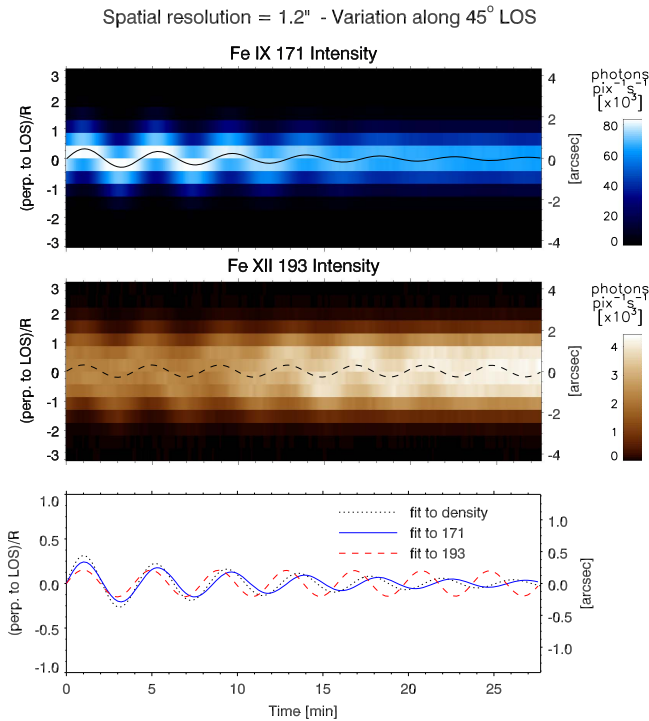
Figure 4. Time–distance diagrams for a slit in the same configuration as in Figure 1, targeting an imaging instrument such as *SDO*/AIA. The damping profile is overlaid on each diagram, calculated by first fitting a Gaussian to the profile at each time step from which the centroid is obtained. Then we fit an exponentially damped cosine to the centroid locations rather than a Gaussian damping profile since the transition from Gaussian to exponential damping is expected after two periods (Pascoe et al. 2015; also, this allows direct comparison to the observational reports). The fits are reproduced in the lower panel, in which the damping to the density is also shown. The latter is produced by integrating the density cross-section at the loop apex along the same LOS ray (45°), removing the background component, and degrading the spatial resolution to $1''2$. We then apply the same fitting procedure as that used for emission lines.

instability. The Alfvén waves therefore act as an energy reservoir for the TWIKH rolls, which persist over time, leading to the decay-less oscillation.

A shorter period is found for the boundary line and is due to phase mixing. Indeed, the azimuthal Alfvén waves in the boundary layer have an increasingly higher phase speed the farther they are from the loop core. Since it is these waves that are enhanced due to resonant absorption and that become K-H unstable, their signal becomes dominant in the boundary line. The fit to the density from the numerical model ends up with a shorter period than that obtained from the core line. This is because the density profile is influenced by the KHI dynamics, which broaden the flux tube, even though the small-scale structure produced by the instability is unresolved. Accordingly, when fitting only the central section of the flux tube along the oscillation axis, which is minimally influenced by resonant absorption and by the KHI, we obtain a period of 256 s, closer to that obtained from the core line.

The out-of-phase behavior between the core and boundary lines is ultimately due to the same effect that leads to the out-of-phase behavior between the LOS velocity and the POS motion seen in the core line (Antolin et al. 2015), explaining the observations by Okamoto et al. (2015). The difference in oscillation period between the core and boundary lines can be used to obtain an estimate of the density at the location of

emission in the boundary layer and also to estimate the density contrast between the loop and the external corona. The period observed with the boundary line (here Fe XII 193 Å) satisfies $P_b = 2L/v_{A_b}$, corresponding to the period of azimuthal Alfvén waves dominating the signal, propagating with speed $v_{A_b} = B/\sqrt{4\pi\rho_b}$. Then $\rho_b = B^2 P_b^2/(16\pi L^2)$. Since the plasma β is low, we can approximate the kink speed as $c_k = \sqrt{2/(1 + \rho_e/\rho_i)}\,v_{A_i}$ and we have $P_k = 2L/c_k$, where P_k is the period of the kink speed, which is to a large accuracy the observed period with the core line. Using these equations to replace the magnetic field we obtain:

$$\frac{\rho_b}{\rho_i} = \frac{1}{2}\left(1 + \frac{\rho_e}{\rho_i}\right)\left(\frac{P_b}{P_k}\right)^2. \quad (1)$$

Replacing with the observed values for P_b and P_k, and assuming that ρ_e and ρ_i are known, we obtain $\rho_b \approx 1.73 \times 10^9\,\mu m_p\,\text{g cm}^{-3}$. The average location (in time and angles) in the boundary corresponding to this density has a temperature of 1.83×10^6 K, very close to the maximum formation temperature of the line. From Equation (1) we can provide an upper limit to the density contrast:

$$\frac{\rho_e}{\rho_i} < \min\left\{\frac{(P_b/P_k)^2}{2 - (P_b/P_k)^2}, \frac{2 - (P_b/P_k)^2}{(P_b/P_k)^2}\right\}, \quad (2)$$

which gives a lowest upper limit of 0.76 (the true value being 0.34).

These results open several possibilities for MHD seismology of the loop shell structure. Indeed, the KHI broadens the density profile, regardless of its initial shape, and the plasma emissivity at a particular temperature in the boundary ends up coming from a small dynamic range. Multiple periods can thus be detected using multiple channels sensitive to different temperatures in the boundary, leading to a temperature-dependent density and the radial structure of a loop (as suggested also by Verth et al. 2010; Fedun et al. 2011). Therefore, this technique also allows us to probe the difference in temperature between loops and their surroundings.

Our model assumes that the loop is colder than the ambient corona. Note that this model differs minimally from a model in which the loop is both hotter and denser than the ambient corona. Indeed, both the resonant properties and KHI onset in the loop remain largely the same. For example, in a model with an ambient temperature of 1 MK and an internal loop temperature of 1.5 MK, similar forward modeling results would be obtained with the same pair of emission lines, except the results corresponding here to the core and boundary lines would be switched. The loop core and boundary would be better visualized with the Fe XII line and the Fe IX line, respectively.

The observed transverse displacement and periods in our model match those observed exhibiting the decay-less kink mode oscillations in coronal loops (Anfinogentov et al. 2013, 2015; Nisticò et al. 2013; Goddard et al. 2016). Our results therefore provide an explanation for these observations. Unfortunately, in these studies only the Fe IX 171 Å line has been used and it is unclear how multi-thermal these loops are and what the temperature difference is with the external corona. The loops shown in these studies present significant intensity changes during their oscillation, in a similar way as the changes observed in our model. Furthermore, the oscillations in our model can appear non-sinusoidal, especially in the first few

periods. Such non-sinusoidal and rather pointy oscillations can be seen in several of the examples provided by Anfinogentov et al. (2013, 2015) and Goddard et al. (2016).

The presence of the KHI and resonant absorption have been demonstrated to be quite robust with respect to density and longitudinal magnetic field variation across the loop, perturbation amplitudes, thickness of the boundary layer, longitudinal flows, and magnetic twist (Antolin et al. 2014; Murawski et al. 2016; J. Terradas et al. 2016, in preparation). The described decay-less effect is limited, however, and will not be observed for strong perturbation amplitudes. This is because the TWIKH rolls that are associated with resonant absorption are always around the flux tube. The combined effect from the coherent motion of vortices and periodic brightening is therefore confined to a transverse layer equal to the loop width, which may explain why such decay-less oscillations are only seen for low amplitudes. On the other hand, for large amplitudes, a negative correlation between damping time and perturbation amplitude has been found by Goddard & Nakariakov (2016), suggesting that non-linear effects such as those described here may still play an important role in the observed overall dynamics of the loop.

REFERENCES

Anfinogentov, S., Nisticò, G., & Nakariakov, V. M. 2013, A&A, 560, A107
Anfinogentov, S. A., Nakariakov, V. M., & Nisticò, G. 2015, A&A, 583, A136
Antolin, P., Okamoto, T. J., De Pontieu, B., et al. 2015, ApJ, 809, 72
Antolin, P., Yokoyama, T., & Van Doorsselaere, T. 2014, ApJL, 787, L22
Arregui, I., Oliver, R., & Ballester, J. L. 2012, LRSP, 9, 2
Aschwanden, M. J., Fletcher, L., Schrijver, C. J., & Alexander, D. 1999, ApJ, 520, 880
De Moortel, I., & Nakariakov, V. M. 2012, RSPTA, 370, 3193
De Moortel, I., Pascoe, D. J., Wright, A. N., & Hood, A. W. 2016, PPCF, 58, 014001
Fedun, V., Verth, G., Jess, D. B., & Erdélyi, R. 2011, ApJL, 740, L46
Goddard, C. R., & Nakariakov, V. M. 2016, A&A, 590, L5
Goddard, C. R., Nisticò, G., Nakariakov, V. M., & Zimovets, I. V. 2016, A&A, 585, A137
Goossens, M., Andries, J., & Aschwanden, M. J. 2002, A&A, 394, L39
Goossens, M., Erdélyi, R., & Ruderman, M. S. 2011, SSRv, 158, 289
Ionson, J. A. 1978, ApJ, 226, 650
Karpen, J. T., Antiochos, S. K., Dahlburg, R. B., & Spicer, D. S. 1993, ApJ, 403, 769
Kudoh, T., Matsumoto, R., & Shibata, K. 1999, Comput. Fluid Dyn. J., 8, 56
Murawski, K., Chmielewski, P., Zaqarashvili, T. V., & Khomenko, E. 2016, MNRAS, 459, 2566
Nakariakov, V. M., Ofman, L., Deluca, E. E., Roberts, B., & Davila, J. M. 1999, Sci, 285, 862
Nisticò, G., Nakariakov, V. M., & Verwichte, E. 2013, A&A, 552, A57
Ofman, L., Davila, J. M., & Steinolfson, R. S. 1994, GeoRL, 21, 2259
Okamoto, T. J., Antolin, P., De Pontieu, B., et al. 2015, ApJ, 809, 71
Pascoe, D. J., Wright, A. N., & De Moortel, I. 2010, ApJ, 711, 990
Pascoe, D. J., Wright, A. N., & De Moortel, I. 2011, ApJ, 731, 73
Pascoe, D. J., Wright, A. N., De Moortel, I., & Hood, A. W. 2015, A&A, 578, A99
Poedts, S., Toth, G., Belien, A. J. C., & Goedbloed, J. P. 1997, SoPh, 172, 45
Terradas, J., Andries, J., Goossens, M., et al. 2008a, ApJL, 687, L115
Terradas, J., Arregui, I., Oliver, R., et al. 2008b, ApJ, 679, 1611
Van Doorsselaere, T., Antolin, P., Yuan, D., Reznikova, V., & Magyar, N. 2016, FrASS, 3, 4
Verth, G., Erdélyi, R., & Goossens, M. 2010, ApJ, 714, 1637
Verwichte, E., Van Doorsselaere, T., White, R. S., & Antolin, P. 2013, A&A, 552, A138
Zaqarashvili, T. V., Zhelyazkov, I., & Ofman, L. 2015, ApJ, 813, 123